Insight into key parameters for fabricating stable single-atom Pt-Ni_x alloy by the reduction environment induced anti-Ostwald effects

Xin Xiao [+],[a, b] Shibo Xi [+],[b] Wenjie Zang,[c] San Hua Lim,[b] Jiajian Gao,[b] Wei Chu,*[a] and Yan Liu *[b]

---

[a] Dr. Xin Xiao,[+] Prof. Wei Chu

School of Chemical Engineering, Sichuan University, No. 24 South Section 1, Yihuan Road, Chengdu, 610065 (China)

E-mail: chuwei1965@scu.edu.cn

[b] Dr. Xin Xiao,[+] Dr. Shibo Xi,[+] Dr. San Hua Lim, Dr. Jiajian Gao, Dr. Yan Liu

Institute of Sustainability for Chemicals, Energy and Environment, A*STAR (Agency for Science, Technology and Research), 1 Pesek Road, Jurong Island, 627833 (Singapore)

E-mail: liu_yan@isce2.a-star.edu.sg

[c] Dr. Wenjie Zang

Department of Materials Science and Engineering, University of California, Irvine, CA92697 (USA)

[+] The authors contribute equally to this work.

Abstract:

Developing single-atom catalysts with superior stability under reduction conditions is essential for hydrogenation / dehydrogenation catalysis and green hydrogen generation. In this contribution, single-atom Pt catalysts were achieved via a reduction environment induced anti-Ostwald approach in the highly confined Ni species (Pt-Ni_x) on nonreducible Al_2O_3 matrix. *In situ* X-ray absorption spectroscopy (EXAFS & XANES) indicated that the isolated Pt-Ni_x metallic bonds, generated at high reduction temperature, dominated the formation of single Pt atoms. A relatively large cluster of metallic Ni would benefit the stabilization of Pt single atom as observed via HAADF-STEM and validated by DFT simulation. Excellent performance on cellulose hydrogenolysis was demonstrated under harsh reductive and hydrothermal conditions, potentially expanded to other hydrogen involved reactions like CO_2 hydrogenation, green hydrogen production from different hydrogen carriers and beyond.

Introduction

Metal oxides supported single-atom catalysts (SACs) have been widely studied due to their maximized atom utilization, distinct electronic properties, and superior activity in a wide sort of reactions.[1] However, the structural stability of SACs under harsh reaction conditions remains a formidable challenge.[2] SACs and small clusters were easy to aggregate due to their high surface free energy.[2b, 3] A wide range of efforts has been tried to stabilize the isolated metal atoms.[3a, 3b, 4] Notably, the strong metal-support interaction derived from the electronic or structural defects on the well-known reducible oxides, such as FeO_x,[3a, 5] CeO_2,[3b, 6] and TiO_2,[4b, 7] was effective to stabilize the single atoms.[1a] However, the nonreducible Al_2O_3, which was commonly applied in the chemical industry field,[8] was seldom reported.

The preparation technique was crucial for the atomically dispersed catalysts. Yan et al. developed a single Pt atom catalyst (0.2 wt%) with strong sinter-resistance, where Pt was confined in the mesoporous channel of Al_2O_3 through a modified sol-gel solvent vaporization self-assembly method.[9] Narula et al. reported Pt SACs (0.18 wt%) prepared by impregnation on sol-gel methodology derived θ-Al_2O_3.[10] Qiao et al. produced SACs of Pt/Fe_2O_3-Al_2O_3 (0.5wt% Pt) by high-temperature calcination under air atmosphere.[2b] In the success mentioned above, the single-atom Pt was achieved in the constrained environment, coordinately unsaturated Al^{3+}, or via the interaction between Pt atoms with reducible Fe_2O_3 in the Al_2O_3 matrix.[11] Nevertheless, in most cases of those SACs, the isolated noble metal atoms were bonded with the oxygen atoms on the Al_2O_3 surface, which was stable under oxidation but prone to aggregate

during reduction.[1a, 1d] The preparation of single atoms, which were stable under the hydrogen atmosphere, remains of significant interest and challenge, especially for the hydrogenation reaction under harsh conditions.

Metal alloys can hold their metal-metal bonds in the reduction environment.[12] Moreover, the emergence of single-atom alloys (SAA) showed promising to fabric stable isolated atoms in the hydrogenation reactions.[13] However, in many cases, the loading of SAA was pretty low (< 1 wt%). The conventional "atom dilute" method often resulted in a core-shell or embedded catalysts with surface-rich non-noble metals.[14] Generally, in the binary alloy system, the composition and particle size of the alloys can be affected by the Ostwald ripening. Especially, under a high temperature, the phase segregation would occur in the alloys and particle size would be redistributed. Normally, the noble metal is sensitive to the reduction temperature and easy to form large particles by high-temperature thermal treatment. How to keep the surface-rich noble metal stable or isolated on the counterpart metal surface during a higher reductive environment is still a challenge. Meanwhile, the stability of those SAA under harsh hydrogenation conditions was still unknown. In this contribution, we successfully created the surface Pt-rich SACs over Al_2O_3 confined Ni surroundings via an *in situ* exsolution approach. By controlling the nickel species confined in Al_2O_3 matrix via the Ni-Al layered double hydroxides (LDHs) as the precursor, the isolated Pt atoms were achieved at atomic level on the confined Ni species via metal-metal bonds (Pt-Ni_x) formation under a high-temperature-reduction atmosphere. The Pt-rich SACs formation mechanism, critical parameters, and the effect of the confined Ni species in Al_2O_3 matrix were unrevealed

by a combined *in situ* X-ray absorption fine structure (XAFS) study, HAADF-STEM verification, and DFT simulation approach. This contribution would shed light on a versatile approach for achieving stable SACs preparation under harsh reduction environments. The demonstrated robust activity indicates the great potential to benefit a wide range of hydrogenation reactions beyond biomass upgrading, potentially contributing to the decarbonization via CO_2 hydrogenation and green hydrogen production from different hydrogen carriers.

Results and discussion

Transformations and speciation of Pt over different Ni-doped Al_2O_3.

Previous studies showed that the second metal in bimetallic catalysts could play specific roles in the base, such as promoting the distribution and reduction.[15] To distribute the metal atoms into isolated ones, a high ratio of non-noble metal / noble metal or low concentration of noble metal was usually applied to prepare single-atom alloys and single-atom catalysts.[13a, 13b, 16] Because the structure (alloy, core-shell, segregation) and components in the bimetallic catalysts impacted the properties and the intrinsic reaction activity,[17] it is critical to track the formation process of single-atom alloys in order to optimize the introduced mode of bimetallic catalysts and, when possible, to optimize the practical component of the effective single-atom catalysts. Nevertheless, there is a big challenge to monitor the dynamic formation process of the bimetallic catalysts or single-atom alloys because the highly dispersed noble metals may not respond to X-ray diffraction or other conventional structural characterization

techniques. To get insight into the formation of the confined NiPt catalysts and obtain stable single-atom Pt catalysts under a reduction environment, in this contribution, *in situ* and *ex situ* EXAFS and HAADF-STEM were applied. Our previous report showed that confined Ni could promote the distribution of Pt at sub-nano level,[18] and the formed Pt surface-rich catalyst demonstrated much-improved capability in the cleavage of H_2 and hydrothermal stability in cellobiose conversion. Herein, we moved one step further in developing the active Pt species at an atomic level. The strategy we adopted is to anchor Ni in Al_2O_3 matrix via its chemical dispersion inside the Ni-Al layered double hydroxides as the precursor for forming NiAl mixed oxides materials (MMO) via calcination. After co-reduction with Pt precursors at a relatively high temperature (550 °C), surprisingly, the atomically dispersed Pt on the Ni-doped Al_2O_3 was obtained, as shown in Fig. 1a-e. With the assistance of highly dispersed Ni species in A_2O_3 matrix, Pt species were atomically dispersed, which was clearly different from the Pt supported on bare Al_2O_3 support, as indicated in Fig. 1f, where Pt was featured on the surface of Al_2O_3 as nanoparticles. The mean particle size of Pt on Pt/Al_2O_3-r (Pt/Al_2O_3 reduced) was 2.4 nm. Based on the HAADF-STEM EDS of 5NiPt1 (Fig. 1a~e), it was deduced that the highly dispersed, confined Ni(0) species would take the responsibility for breaking the Pt-Pt bond into atomical Pt species. Previous reports showed that the single-atom alloy catalyst was usually obtained by the reduction of diluted noble metal in a second non-noble metal precursor.[13, 17b] Because of the dilution of the metal precursors, the loading of atomically-dispersed metal is usually limited to 1 wt%. Furthermore, high-temperature thermal treatment would result in large metal particle

sizes due to the Ostwald ripening.[19] In contrast to the traditional preparation of single-atom alloy, in this work, the confined Ni species in the Al_2O_3 matrix would promote the dispersion of Pt at single atom level at a relatively high loading of 1 wt%.

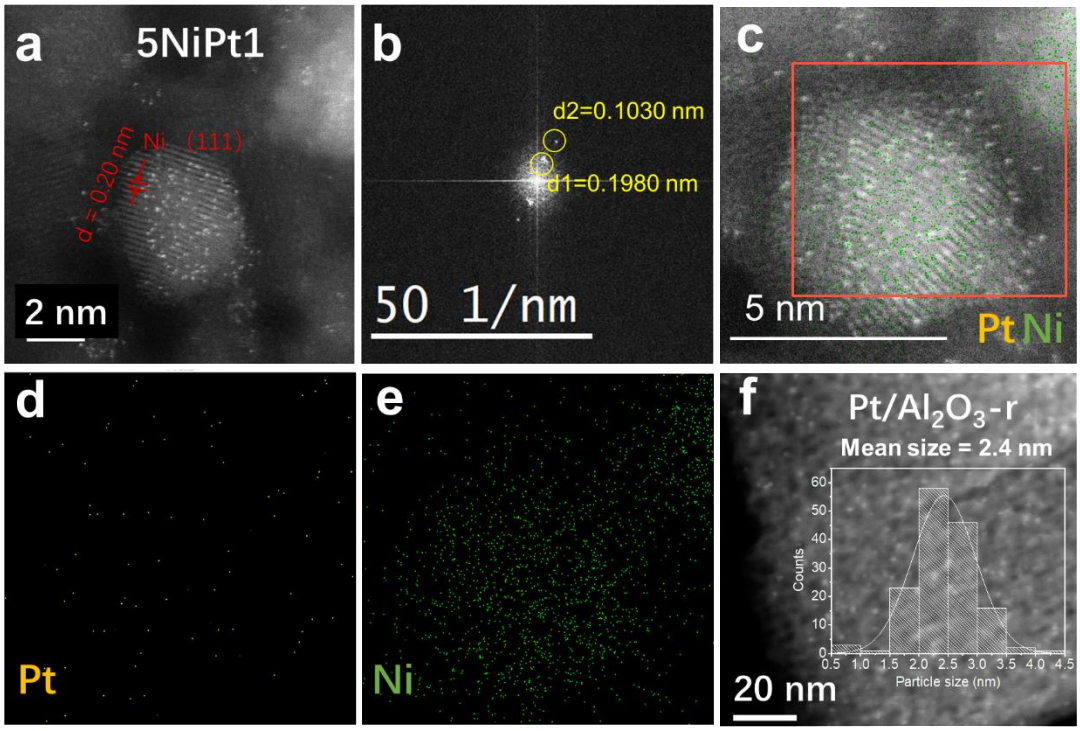

Fig. 1 a, HAADF-STEM image of 5NiPt1 catalyst. **b**, Selected area transmission electron diffraction pattern. **c** ~ **e**, HAADF-STEM EDS of 5NiPt1, element Pt (**d**) and Ni (**e**). **f**, TEM image of Pt/ Al_2O_3-r.

Figure 2 shows the Fourier transforms (FT) of Extended X-Ray Absorption Fine Structure (EXAFS) signals and X-ray Absorption Near-Edge Structure (XANES) profiles (Fig. 2 a,b) collected at the Pt L_3 edge over different Al_2O_3 supported Pt-based catalysts. An intense peak is clearly observed at 1.78 Å for the unreduced Pt/Al_2O_3-p (Pt/Al_2O_3 as prepared, Fig. 2a), indicating that Pt has been loaded on Al_2O_3 via its Pt-

Cl bond after removing the moisture.[9] After *in situ* reduction at 550 °C, the first intensive peak at 2.24 Å is getting visible over Pt/Al_2O_3-r (Pt/Al_2O_3 reduced), implying the reduction of Pt species and the formation of Pt-Pt bond similar to that of Pt foil. xNiPt1 (x = 0.5, 2, 5, 15) were chosen as model catalysts to investigate the optimal Ni content for the formation of single-atom Pt catalysts. It was shown that the peak position for Pt-Pt bond left-shifted from 2.40 to 2.14 Å with the increase of Ni content, indicating the break of Pt-Pt bond and disorder of the Pt nanostructure with small size.[20] In particular, for samples 5NiPt1 and 15NiPt1, the peak position for Pt-Pt bond shifted to the lowest position at 2.08 Å, which indicated the high dispersion of Pt species. As for the Pt L_3-edge XANES profiles (Fig. 2b), the decreased intensity of the white line and similar shape of that on Pt foil further confirm the reduction of Pt species over xNiPt1 catalysts. Absorption edge energy denotes the threshold energy (E_0) for electron excitation by X-ray from 2p to 5d orbitals for the Pt L_3-edge XANES.[1b, 14] The red shift of absorption energy on xNiPt1 compared with Pt foil indicated the electron status altering and the formation of Pt-Ni alloy in the catalysts (Fig. 2c), which was consistent with the reported Pt@NiPt alloy samples.[14]

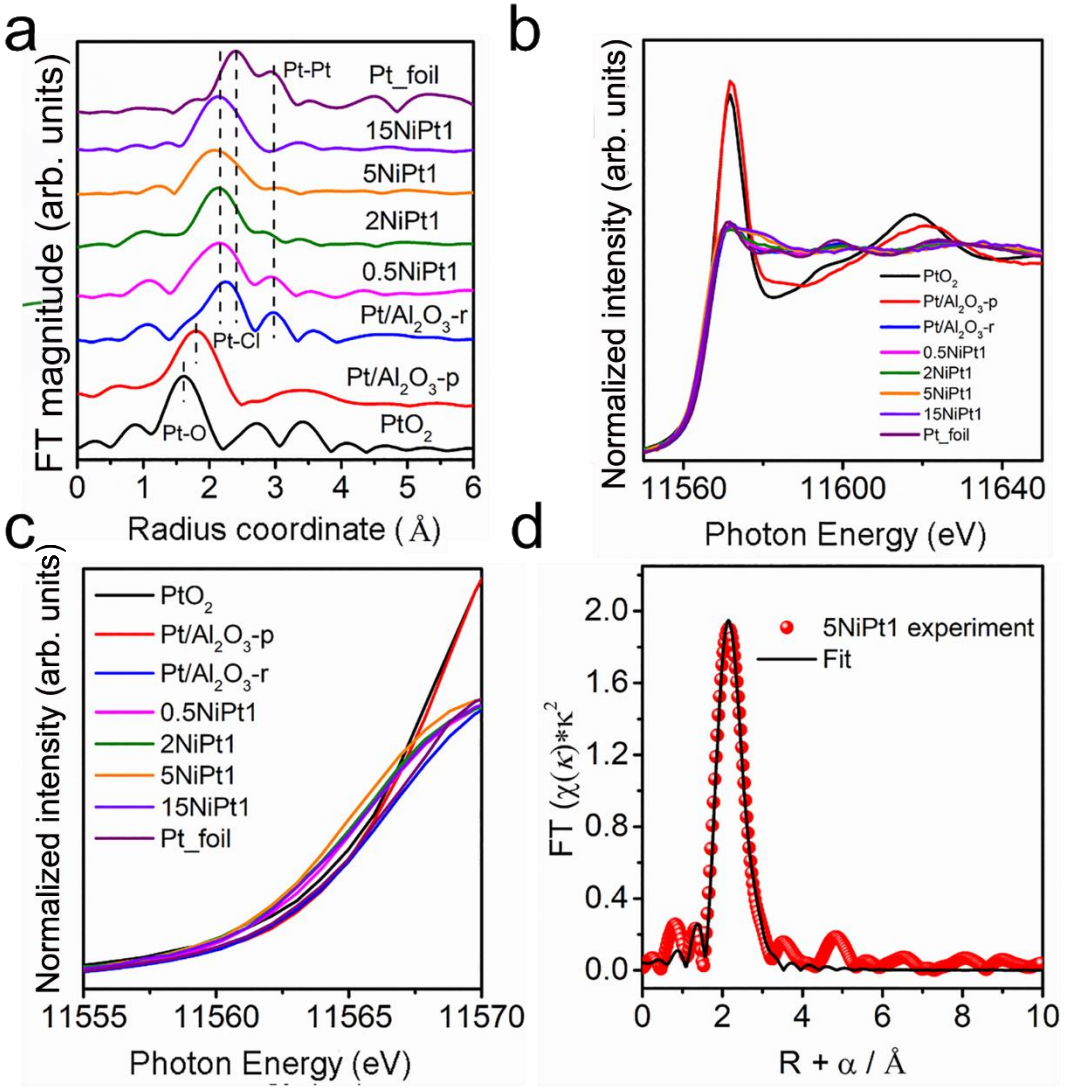

Fig. 2 a, Pt L_3-edge FT-EXAFS for Pt/Al_2O_3 samples and xNiPt1 catalysts (x = 0.5, 2, 5, 15). Pt foil and standard PtO_2 were used as references. **b**, Pt L_3-edge XANES spectra for Pt/Al_2O_3 samples and xNiPt1 catalysts (x = 0.5, 2, 5, 15). Pt foil and standard PtO_2 were used as references. **c**, Enlarged version of Pt L_3-edge XANES spectra for Pt/Al_2O_3 samples and xNiPt1 catalysts (x = 0.5, 2, 5, 15) at the energy range of 11555 – 11570 eV. **d**, FT-EXAFS curves of 5NiPt1 with fitting.

Table 1 The EXAFS fitting results of Pt in different xNiPt1 catalysts [a]

sample	Shell	CN	R(Å)	σ^2(10^{-2} Å^2)	ΔE_0 (eV)	R-factor (%)
Pt foil	Pt-Pt	12.0	2.76	0.004	9.5	0.3
0.5NiPt1	Pt-Pt	6.2	2.71	0.006	7.1	3
	Pt-Ni	4.4	2.58	0.010		
2NiPt1	Pt-Pt	4.1	2.67	0.007	6.5	0.8
	Pt-Ni	3.7	2.55	0.010		
5NiPt1	Pt-Pt	5.1	2.73	0.003	9.0	0.8
	Pt-Ni	5.9	2.53	0.003		
15NiPt1	Pt-Ni	8.8	2.53	0.005	8.6	1.0

[a] CN is the coordination number for the absorber-backscatter pair, *R* is the average absorber-backscatter distance, σ^2 is the Debye-Waller factor, and ΔE_0 is the inner potential correction. The accuracies of the above parameters are estimated as CN, ±20%; R, ±1%; σ^2, ±20%; ΔE_0, ±20%. The data range used for data fitting in K-space (Δk), and R-space (ΔR) are 3.0 – 12.0 Å^{-1} and 1.0 – 2.9 Å.

To uncover the change of Pt coordination environment in xNiPt1 catalysts, the EXAFS fitting results are summarized in Table 1. Compared with the metallic Pt species in Pt-foil, the xNiPt1 samples showed a smaller Pt-Pt coordination number (< 12) and shortened Pt-Pt distance (< 2.76 Å), suggesting that the Pt centers in the xNiPt1 samples are getting highly dispersed. The Pt-Pt coordination is more unsaturated and the Pt-Pt metallic bond is weaker. As for the Pt-Ni shell, the distance of Pt-Ni shortened (from

2.58 to 2.53 Å) with increase of the Ni content in the xNiPt1 samples. Moreover, the ratio of shell Pt-Pt/Pt-Ni coordination number was decreased as 0.5NiPt1 (6.2/4.4 = 1.41) > 2NiPt1 (4.1/3.7 = 1.11) > 5NiPt1 (5.1/5.9 = 0.86) > 15NiPt1 (0), suggesting the enhanced dispersion of Pt in the Ni surroundings. Increasing Ni amounts from 5NiPt1 to 15NiPt1, Pt is closing to an atomic dispersion. No Pt-Pt bond exists in the 15NiPt1 sample, strongly suggesting a Ni-promoted single-atom Pt dispersion via Pt-Ni_x metallic bond stabilization.

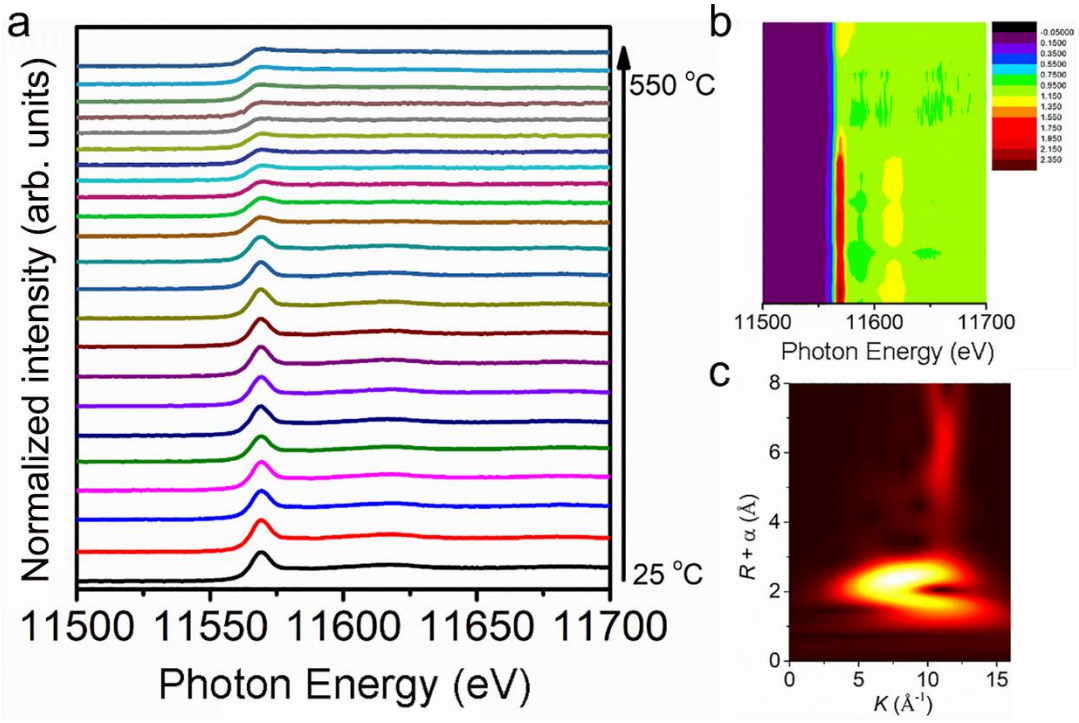

Fig. 3 a, **b** The *in situ* Pt L_3-edge XANES characterization of the 5NiPt1 catalyst. **c** Wavelet Transformation for the k^2-weighted EXAFS of sample 5NiPt1. The first 19 spectrums were collected at 25 min intervals, while the last four spectrums were collected at 12.5 min intervals.

To identify the critical parameter for forming atomically dispersed Pt-Ni_x, the *in situ*

EXAFS experiments were performed on sample 5NiPt1. In the XANES spectra (Fig. 3a and Fig. 3b), the white-line intensity at the Pt L_3-edge decreases continuously with an increase in the reduction temperature. It was shown that the white-line intensity of Pt L_3-edge keeps nearly constant above 400 ºC, suggesting that the necessity of minimum reduction temperature is over 400 ºC. Moreover, the comparison of the wavelet transformed plot of reduced 5NiPt1 and Pt foil (Supplementary Fig. 1) demonstrates the existence of Pt single atoms. These results display strong evidence to disperse Pt atoms into single atoms by *in situ* reduction of confined-Ni mobilizing Pt species.

The effect of confined Ni species on the formation of single-atom Pt catalyst.

Supplementary Fig. 2 showed the XRD patterns of uncalcined xNiAl-p and calcined xNi-MMO samples. The prominent peaks in Supplementary Fig. 2a were ascribed to the phase of $Al(OH)_3$. As for the xNi-MMO (Supplementary Fig. 2b), typical diffraction peaks of γ-Al_2O_3 (2θ = 37.3º, 45.7º, 67º) were observed as the main phase in those samples.[21] While for 15Ni-MMO, two tiny diffraction peaks (2θ = 43.4º, 63.2º) corresponding to the phase of NiO appeared due to the high loadings of Ni.[22] A weak diffraction peak of spinel-$NiAl_2O_4$ was observed on the calcined 5Ni-MMO.[15b, 22] To further understand the effect and structure change of Ni on the formation of Ni-Pt single-atom alloys, the Ni K-edge XAFSs of xNiPt1 samples were collected as shown in Fig. 4 (a ~ c). Fig. 4a indicated the FT-EXAFS signals collected at the Ni K-edge,

while the optimal-fitted EXAFS results of Ni were summarized in Table 2. In Fig. 4a, the peak at 2.52 Å over 5Ni-MMO was ascribed to the Ni-Ni formation during the reduction process, further confirmed via the optimal-fitted results in Table 2. Along with an increase of Ni loadings in 0.5NiPt1 and 2NiPt1, the peak at 2.52 Å becomes broader and gradually disappears in 5NiPt1 and 15NiPt1 samples, suggesting the loading reaches 5 wt% and 15 wt%. The new peak at 2.17 Å occurs over the 5NiPt1 sample, which may be ascribed to the formation of Ni-Pt. As summarized in Table 2, compared to the bulk Ni foil, the xNiPt1 sample has a decreased Ni-Ni coordination number (< 12), and a similar Ni-Ni distance, suggesting the constrained environment of Ni foil and thus the reduction of Ni species in xNiPt1 samples. In particular, with the increase of Ni content, the Ni-Ni coordinate number becomes larger, indicating the growth size of Ni cluster under the confined environment. To further study the reduction of Ni, the EXAFS of Ni K-edge and XPS test results of xNiPt1 catalysts were shown in Fig. 4b ~ Fig. 4d.

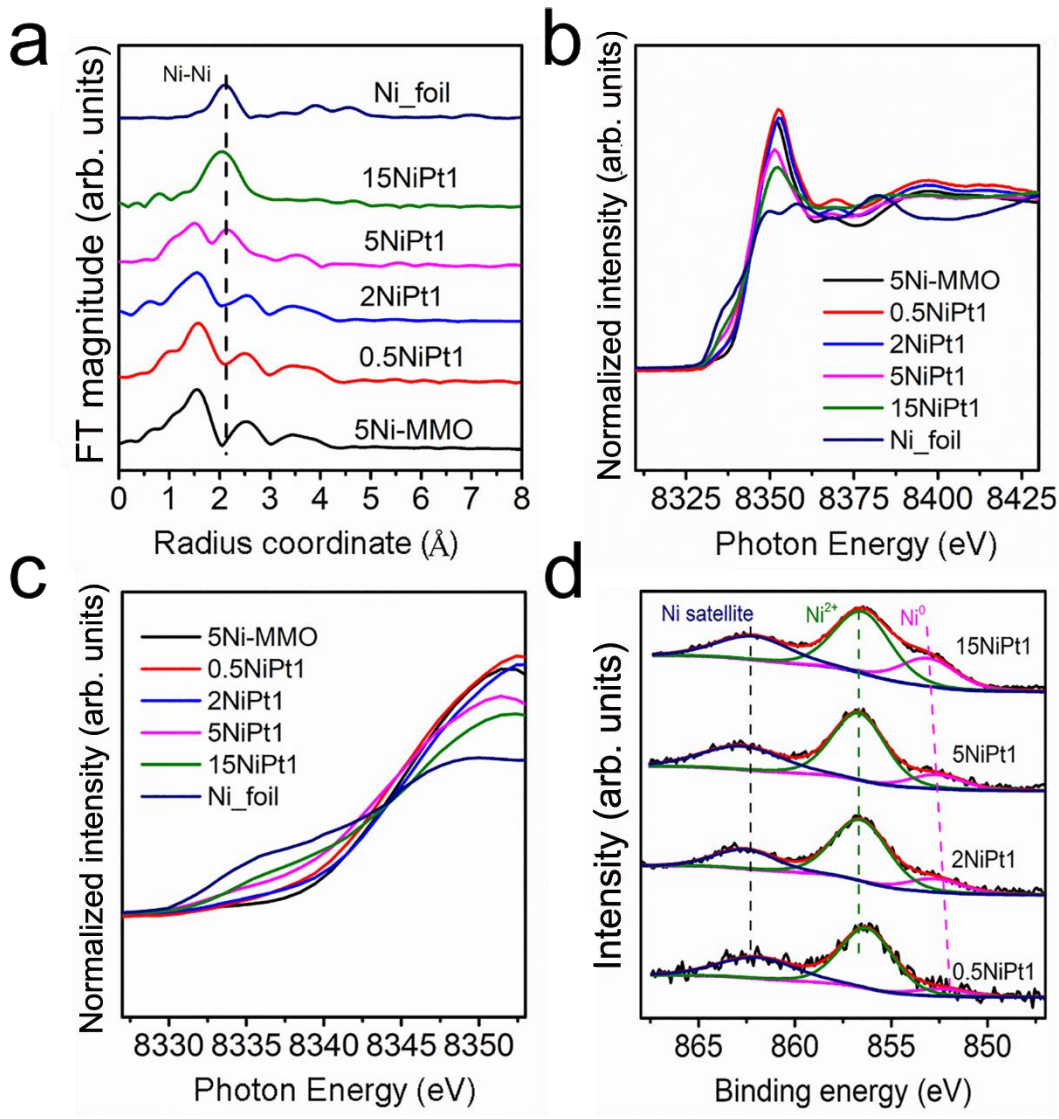

Fig. 4 a, Ni K-edge FT-EXAFS for xNiPt1 samples. Ni foil and 5Ni-MMO were used as references. **b**, Ni K-edge XANES for different 5NiPt1 samples. Ni foil and Pt-free 5Ni-MMO were used as references. **c**, High resolution Ni K-edge EXAFS for different 5NiPt1 samples. **d**, Ni 2p XPS spectra for xNiPt1 (x = 0.5, 2, 5, 15) samples.

As shown in Fig. 4b, the white line intensity of xNiPt1 was lower than that of 5Ni-MMO, indicating the reduction of Ni species in those catalysts. However, different from the double-peak around 8350-8360 eV in the Ni foil, which is the characteristic of fcc

metallic Ni, the white lines shift to higher energy in the xNiPt1 samples (Fig. 4c), indicating that Ni was partially oxidized in the xNiPt1 catalysts, which was similar to the reported Ni-rich Pt_1-Ni bimetallic catalysts.[14] Furthermore, with the content of Ni increasing in the xNiPt1 catalysts, the pre-edge feature of Ni at 8334 eV was close to that in the Ni foil (Fig. 4c), suggesting the generation of more Ni (0) species. X-ray photoelectron spectroscopy (XPS) (Fig. 4d) revealed the binding energies (BE) of 856.4 and 852.0 eV for Ni 2p3/2 and Ni 2p1/2, corresponding to the Ni^{2+} and Ni^0 species, respectively.[23] The negative shift of binding energy for Ni^0 species with the increase of Ni loading implied the electron transfer from Pt to Ni,[20] which may promote the reduction of Ni. The summarized $Ni^0/(Ni^{2+} + Ni^0)$ ratios in Supplementary Table 3 further confirmed this promoted Ni reduction in the xNiPt1 samples. Integrating with the STEM results and XAS characterization on Pt species, the special Pt-Pt bond length of 5NiPt1 can be ascribed to the formation of single-atom Pt on confined Ni in Ni-Al oxide matrix. The shrink of Ni-Ni and Pt-Pt bonds in different xNiPt1 showed that the reduction of confined Ni species could promote Pt dispersion.

Table 2 The optimal-fitted EXAFS results of Ni in different xNiPt1 catalysts [a]

sample	Shell	CN	R(Å)	σ^2(10^{-2} Å^2)	ΔE_0 (eV)	R-factor (%)
Ni foil	Ni-Ni	12.0	2.48	0.006	0.5	0.06
5Ni-MMO	Ni-O	5.7	2.02	0.006	1.9	0.3
	Ni-Ni	1.4	2.58	0.009	1.6	
0.5NiPt1	Ni-O	4.2	2.0	0.005	1.3	0.5
	Ni-Ni	2.3	2.44	0.009	7.6	
2NiPt1	Ni-O	4.7	2.0	0.007	0.9	0.4
	Ni-Ni	3.8	2.5	0.012	2.0	
5NiPt1	Ni-O	3.5	2.02	0.006	1.4	0.2
	Ni-Ni	4.5	2.49	0.009	2.8	
15NiPt1	Ni-O	1.7	2.01	0.004	2.7	0.8
	Ni-Ni	6.6	2.48	0.006	2.5	

[a] CN is the coordination number for the absorber-backscatter pair, R is the average absorber-backscatter distance, σ^2 is the Debye-Waller factor, and ΔE_0 is the inner potential correction. The accuracies of the above parameters are estimated as CN, $\pm$20%; R, $\pm$1%; σ^2, $\pm$20%; ΔE_0, $\pm$20%. The data range used for data fitting in K-space (Δk), and R-space (ΔR) are 3.0 ~ 12.0 Å^{-1} and 1.0 ~3.2 Å.

DFT simulation on the stability of isolated Pt atom dependence on Ni particle size.

DFT calculation was performed in this work to identify the appropriate confined cluster for preparing Pt SACs. To decipher the process for atomic Pt formation, we modeled different Ni clusters (Ni_{13}, Ni_{55}) containing two embedded Pt single-atoms. The anti-Ostwald behaviors can be understood by studying the energy barrier in the dimerization process. Fig. 5 shows the reaction pathway of Pt-embedded Ni clusters undergoing Pt_2-dimerization. At the initial stage, both the Pt_1-Pt_1-Ni_{11} and Pt_1-Pt_1-Ni_{53} clusters represented two adjacent, single Pt atoms embedded in the nickel clusters. The barrier energies of Pt_2-dimerization were determined to be 24.4 and 80.4 kcal mol^{-1} for the Ni_{13} and Ni_{55} clusters, respectively. In other words, the larger the Ni clusters, the embedded single Pt atoms will be more stable, isolated, and less likely to form dimers. The positive reaction energies for the Pt_2-dimerization indicated that the process is endothermic and thermodynamically unfavorable. These DFT calculations were qualitatively similar to our experimental observations that more active Pt single atoms were embedded in higher loading of the nickel catalysts.

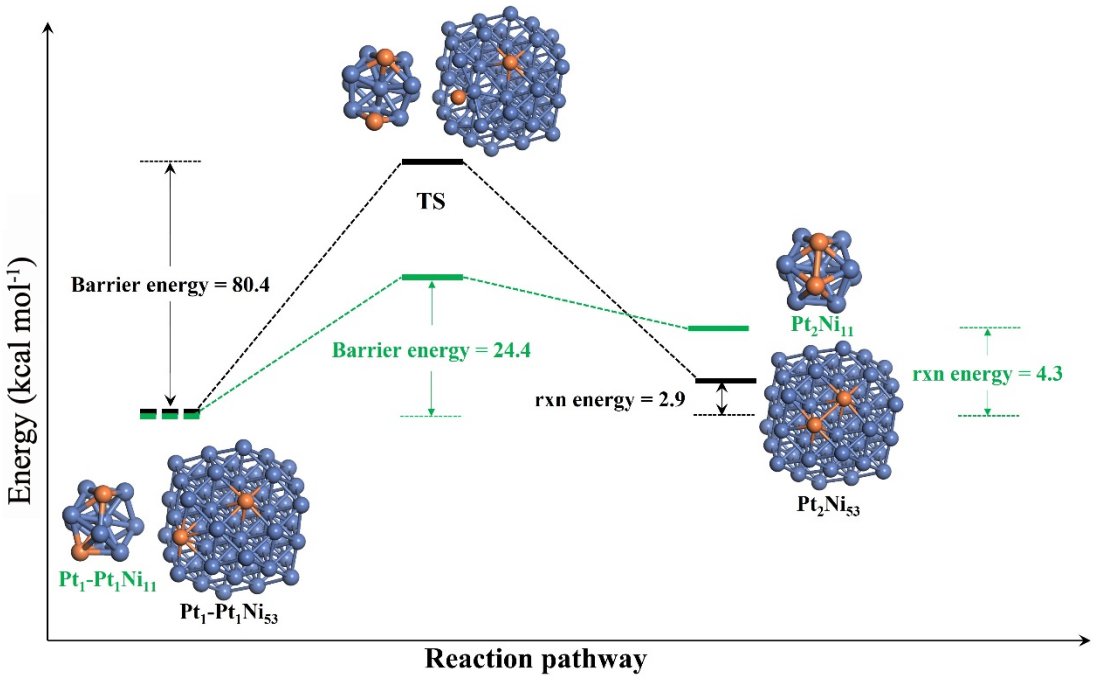

Fig. 5 Reaction pathway of Pt_2 dimerization on Pt_2-Ni_{11} (green lines) and Pt_2-Ni_{53} (black lines) clusters as determined by LST/QST method (Energy diagrams are not drawn to scale; rxn energy refers to reaction energy).

Plausible formation mechanism of atomically dispersed Pt in confined Ni cluster.

Via integrating the characterization results, we proposed the plausible formation mechanism of single-atom xNiPt1 by the reduction-environment induced anti-Ostwald effects as shown in Fig. 6. In catalyst preparation, the precursor of Pt-Cl species was loaded on the confined Ni-Al mixed metal oxides via impregnation method. Normally, the Pt-Cl bonds were easily cleaved in the hydrogen-rich environment by the formation of H-Cl bond (Step I). This process usually took place at a relatively low temperature (300 ~ 400 °C).[20] Due to the confined environment of NiO in Al_2O_3 matrix, its reduction to metallic Ni species can only be obtained at a temperature higher than 500

°C with limited amounts (Step II). [15b, 24] With the assistance of easily reduced Pt species, the adsorbed hydrogen (H_{ad}) spilled over from Pt-H_{ad} surface and promoted the reduction of NiO. Owing to the strong interaction between Ni and Al_2O_3, the aggregation of Ni was halted and the Pt clusters were further dispersed into single atom through the formation of Pt-Ni_x metallic bonds (Step III). Here, Al_2O_3 support provides a confined environment and periodic matrix to isolate Ni clusters as a platform for Pt dispersion. The relatively high content of Ni metallic atom (x) will enhance the stabilization of Pt atom on the confined Ni species in non-reducible Al_2O_3 matrix (supported by Fig. 1 STEM images, Fig. 2 EXAFS & XANES spectra, Table 1 EXAFS fitting, and Fig. 5 DFT simulation).

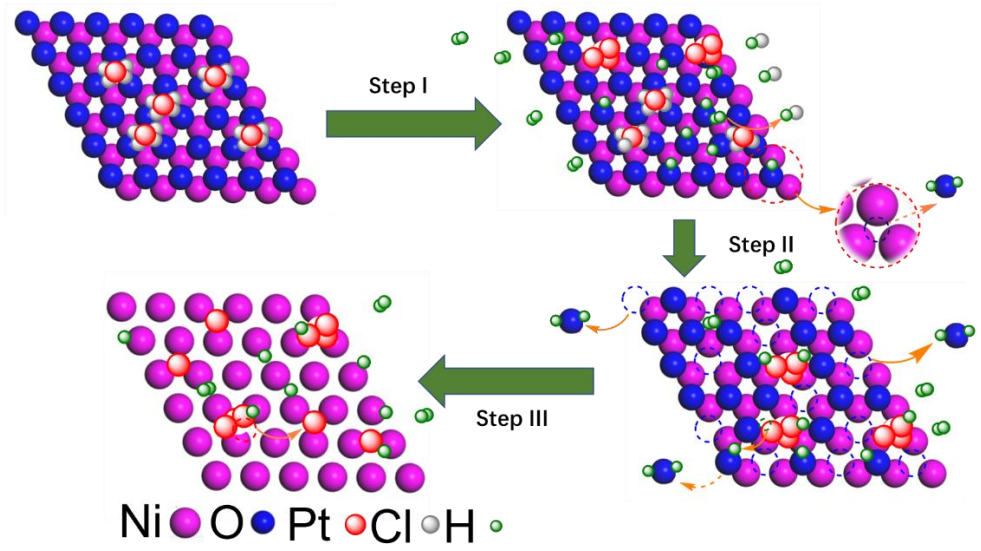

Fig. 6 Schematic illustration for the formation of the single-atom Pt-Nix samples

Catalytic application.

Since the xNiPt1 catalyst was prepared in a relatively high-temperature and reducing atmosphere, it was expected to own promising performance in catalyzing

hydrogenation reactions. Here, we took a one-pot conversion of cellulose into polyols as a probe hydrogenation reaction. One-pot conversion of cellulose as a promising route for sustainable production of fuels and chemicals has been studied for many years. The main product, i.e. hexitols, was widely used in food chemistry and taken as essential platform products to produce energy chemicals.[12a, 15b, 25] However, due to the highly functionalized feature of cellulose, harsh conditions like strong acid/basic media, high temperature, and pressure were applied when transforming the cellulose into liquid chemicals.[26] A big challenge in the durability of catalysts remains. The catalytic performance in Fig. 7a showed that all the xNiPt1 catalysts could afford 100% conversion of cellulose. The content of Ni would promote the hexitol yield, and it can reach the highest 69% over catalyst 5NiPt1. According to the literature,[25, 26b] the cellulose hydrogantion reaction would go through the hydrogenolysis and C-C/C-O cleavage process. The activities displayed in Fig.7a would be ascribed to a synergetic effect between Ni and Pt. With the increase of Ni content, the metallic Pt becomes fully exposed, leading to a plateau of reaction activities. Fig. 7b showed that the catalytic performance of 5NiPt1 stood out of the reported catalysts at the relatively high conversion of cellulose and hexitol yield. The recycle test in Supplementary Fig. 3 further showed the stability of 5NiPt1 in this liquid reaction. After the third recycling, the cellulose conversion still keeps at 100%, while the hexitol yield remains high (65%). Those results demonstrated the great activity of such catalyst in a harsh reducing environment, providing a novel route for biomass upgrading using highly stable single-atom catalysts.

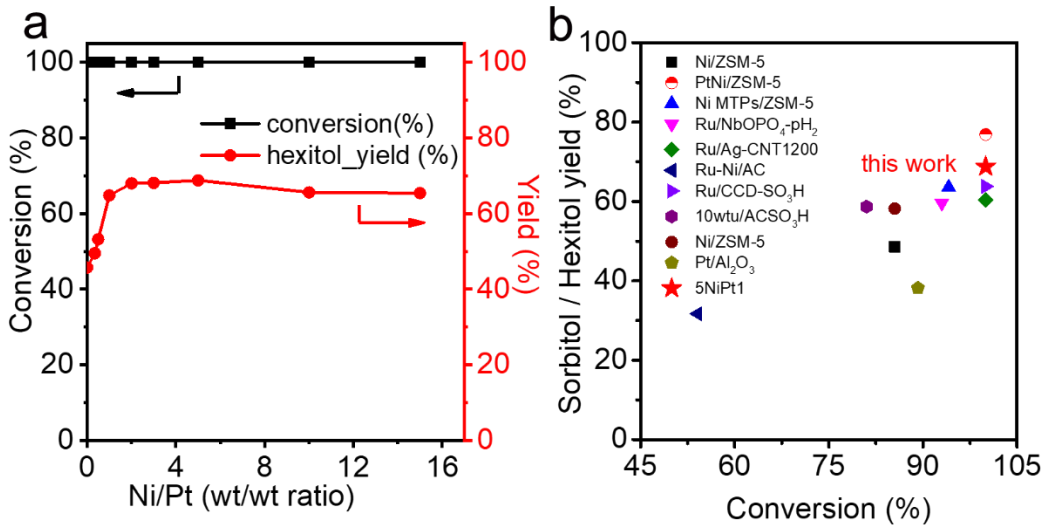

Fig. 7 a, Catalytic performance of different xNiPt1 samples. Reaction condition: 0.255g cellulose, 0.075g catalyst, 30 mL DI water, 50 bar H_2 pressure (room temperature), 200 ^{o}C, 6 h. **b,** comparison of cellulose conversion and sorbitol or hexitol yield over reported catalysts and 5NiPt1 in this work.

Conclusion.

We report an *in situ* reduction induced anti-Ostwald approach to synthesize the stable Pt single-atom catalysts on highly confined Ni species in nonreducible Al_2O_3 matrix. Results showed that the surface Pt species would promote the reduction of NiO in NiAl-MMO, while the reduced and confined metallic Ni species can inversely promote the isolation of Pt atoms by the constrained Pt-Ni_x metallic bonds. Remarkable catalytic activity and stability were achieved on this catalyst towards cellulose hydrogenolysis under harsh hydrogenation conditions. *In situ* EXAFS experiment and DFT calculations revealed that the isolated Pt atoms were dependent on the confined size of the Ni cluster. Generally, the low content of Ni-doping would result in small clusters, where Pt was

prone to aggregate. The relatively high loading of Ni content can result in larger Ni clusters to stabilize the isolated Pt atoms. The Pt SACs can only form uniformly at high Ni loading (5wt% and above) over Al_2O_3 supports due to their appropriate surface Ni species. Since Ni is replaceable by other transitional metal atoms, such as Co and Cu, etc., our *in situ* reduction induced anti-Ostwald approach approach may afford a generic route to synthesize and understand high loading Pt SACs over diverse supports, operating under harsh hydrogenation / dehydrogenation conditions.

Experimental section

Materials Preparation

NiAl-hydroxides precursors (NiAl-p) were prepared by modified co-precipitation as previous reported literature.[15b] Typically, nickel nitrate and aluminum nitrate were dissolved into 100 mL deionized (DI) water to form homogenous solution A. 0.15 M of 100 mL Na_2CO_3 and 1.0 M of 100 mL NaOH were prepared and marked as solution B and C, respectively. The co-precipitation was conducted in a three-neck bottle at 60 °C. Firstly, solution A was dropwise into the 100 mL Na_2CO_3 in the three-neck bottle under stirring. During coprecipitation, the pH value in the three-neck bottle was controlled at 10 by injecting certain amount of 1.0 M NaOH. After coprecipitation, the slurry was kept stirring for 1 hour and subsequently aged at 60 °C for 24 h. The aged solution was suffered filtering, washing and drying to obtain sample xNiAl-p (x = 0%, 0.5%, 2%, 5%, 15%) with different Ni content. Support xNiAl-MMO (mixed metal oxides) were derived from xNiAl-p by calcining the dried xNiAl-p at 500 °C for 3h in the static air.

xNiPt catalysts were prepared by conventional impregnation and in situ reductionist approach. For instance, certain amount of 0.97 M H_2PtCl_4 was dropped into 20 mL DI water. 1.0 g of prepared xNiAl-MMO was added to the solution. The solution was kept stirring for 2 hours at room temperature. Afterwards, water in the solution was removed by rotary vaporization at 60 ºC. The obtained sample was then dried in 100 ºC oven for 14 hours and reduced at 550 ºC for 1h in the flowing H2-Ar mixed gas at 50 sccm.

Materials Characterization

Powder X-ray diffraction (XRD) patterns of the prepared precursors and the calcined mixed oxides were collected on a powder diffractometer (Bruker D8 Advance X-ray) with a Cu-kα source (k_α= 0.514 nm) in the 2θ range between 5º to 85º. X-ray photoelectron spectroscopy was conducted on a XSAM800 XPS equipped with an Al-kα source(hv = 1486.6 eV). The obtained XPS spectrum were calibrated with the C1s peak at 284.6 eV. Low-temperature N_2 adsorption/desorption isotherms were collected to determine the specific surface area at -196 ºC. Before the test, all samples were degassed at 200 ºC for 24 h. The specific area was calculated by the reported Brunauer-Emmett-Teller (BET) equation, and the pore-size distribution was obtained from the desorption branch of the isotherms with the Barrett-Joyner-Halenda (BJH) method. Scanning transmission electron microscopy (STEM) and energy-dispersive X-ray spectroscopy (EDS) measurements were carried out at 80 kV using a JEOL ARM200F equipped with the ASCOR aberration corrector, cold field emission gun, Gatan

Quantum ER spectrometer, and Oxford X-max 100TLE SDD EDS. The images were collected with a half-angle range from ~ 85 to 280 mrad, and the convergence semiangle was set at ~ 30 mrad. The loading of Pt and Ni was measured on the Agilent VISTA-MPX inductively coupled plasma-optical emission spectroscopy (ICP-OES). The X-ray absorption near edge structure (XANES) and the extended X-ray absorption fine structure (EXAFS) tests of Pt L_3-edge and Ni K-edge of the samples were measured at the XAFCA beamline of Singapore Synchrotron Light Source (SSLS).[27] The storage ring of SSLS operated at E = 700 MeV and Imax = 200 mA. The radiation was monochromatized by the Si (111) double-crystal monochromator. Pt foil and Ni foil were taken as reference for energy calibration. The EXAFS oscillations, $x(k)$, were extracted and anlayzed using the Demeter software package.[28]

DFT calculation

All the theoretical caluculation in this work were carried out using Material Studios 8.0 with Dmol3 DFT package. We modeled different Ni clusters (Ni13, Ni55) containing two embedded Pt single-atoms/Pt-dimer to study the energy barrier for the dimerization process. The exchange-correlation potential was described by the Perdew-Burke-Ernzerhof (PBE) generalized gradient approach (GGA). Double precision numerical basis sets augmented with polarization functions (DNP) were used to describe the valence electrons, while the core electrons were treated with All Electron Relativistic pseudo-potential. The transition state (TS) structure search was performed to gain insight into the barrier of hydrogen dissociative chemisorption by the LST/QST method.

This method begins by performing a linear synchronous transit (LST)/optimization calculation. The transition state (TS) approximation obtained was used to perform a quadratic synchronous transit (QST) maximization. On the basis of that maximization point, another constrained minimization was performed, and the cycle was repeated until a stationary point was located.

Catalytic performance test

One-pot cellulose conversion was used as a probe reaction for the catalytic performance test of xNiPt1 catalysts. The catalytic reaction test was carried out in a 100 mL stainless Parr reactor. Typically, 75 mg of pre-reduced catalyst, 0.255 g cellulose, and 30 mL DI water were loaded into the Parr reactor together. The reactor was first purged by H_2 gas five times to remove the air in the system, and then 50 bar hydrogen was introduced at room temperature. The reaction was performed at 200 °C for 6 h. Subsequently, the reactor was quenched in the ice bath. The collected solution was centrifugated, and the liquid phase was analyzed by an HPLC instrument equipped with an RI detector. Hexitols are the goal product in this work. The conversion of cellulose and yield of hexitols was chosen as the main indicators in this contribution.

Cellulose conversion and hexitol yield were calculated as the previous reported[4] as follows:

$$conversion(\%) = \frac{m_b - m_a}{m_b} \times 100\% \quad (1)$$

$$m_a = m_r - m_c \quad (2)$$

$$Heixitol\ yield(\%) = \frac{n_j k_j M_u}{6B_{cellulose}} \times 100\% \quad (3)$$

Here, in equation (1), m_b represents the weight of cellulose before reaction. m_a is the weight of cellulose after reaction, which can be calculated by the equation (2). m_r is the mass of solid mixture after reaction, m_c is the mass of catalyst loaded in the reaction. In equation (3), n_j is the molar amount of the product j, k_j is the carbon number in the product j, and M_u is the relative molecular mass of $C_6H_{10}O_5$ as the constructed cellulose unit.

Acknowledgement

The authors gratefully acknowledge Dr. Kelvin Mingyao Kwok and Ms. Wang Zhan April (ISCE^2, A*STAR, Singapore) to support the TEM and XPS test. The authors thank the Chinese Scholarship Council (CSC) for providing the Ph.D. scholarship (X. Xiao) and ISCE^2 (A*STAR, Singapore) for the financial support.

Keywords: cellulose hydrogenolysis; confined metal-metal bonds; *in situ* EXAFS; single-atom Pt; Pt-Ni catalyst.

Reference

[1] a) A. Wang, J. Li, T. Zhang, *Nat. Rev. Chemistry* **2018**, *2*, 65-81; b) K. Liu, X. Zhao, G. Ren, T. Yang, Y. Ren, A. F. Lee, Y. Su, X. Pan, J. Zhang, Z. Chen, J. Yang, X. Liu, T. Zhou, W. Xi, J. Luo, C. Zeng, H. Matsumoto, W. Liu, Q. Jiang, K. Wilson, A. Wang, B. Qiao, W. Li, T. Zhang, *Nat. Communications* **2020**, *11*, 1263; c) H. Yang, L. Shang, Q. Zhang, R. Shi, G. I. N. Waterhouse, L. Gu, T. Zhang, *Nat. Communications* **2019**, *10*, 4585; d) Y. Ma, Y. Ren, Y. Zhou, W. Liu, W. Baaziz, O. Ersen, C. Pham-Huu, M. Greiner, W. Chu, A. Wang, T. Zhang, Y. Liu, *Angew. Chem., Int. Ed. Engl.* **2020**, *59*, 21613-21619.

[2] a) W. Liu, Y. Chen, H. Qi, L. Zhang, W. Yan, X. Liu, X. Yang, S. Miao, W. Wang, C. Liu, A. Wang, J. Li, T. Zhang, *Angew. Chem., Int. Ed. Engl.* **2018**, *57*, 7071-7075; b) R. Lang, W. Xi, J. C. Liu, Y. T. Cui, T. Li, A. F. Lee, F. Chen, Y. Chen, L. Li, L. Li, J. Lin, S. Miao, X. Liu, A. Q.

Wang, X. Wang, J. Luo, B. Qiao, J. Li, T. Zhang, *Nat. Communications* **2019**, *10*, 1-10.

[3] a) B. Qiao, A. Wang, X. Yang, L. F. Allard, Z. Jiang, Y. Cui, J. Liu, J. Li, T. Zhang, *Nat. Chemistry* **2011**, *3*, 634-641; b) J. Jones, H. Xiong, A. T. DeLaRiva, E. J. Peterson, H. Pham, S. R. Challa, G. Qi, S. Oh, M. H. Wiebenga, X. I. Pereira Hernández, Y. Wang, A. K. Datye, *Science* **2016**, *353*, 150; c) A. W. Xiao-Feng Yang, Botao Qiao, Jun Li, Jingyue Liu, and Tao Zhang, *Acc. Chem. Res.* **2013**, *46*, 1740–1748.

[4] a) X. Ye, C. Yang, X. Pan, J. Ma, Y. Zhang, Y. Ren, X. Liu, L. Li, Y. Huang, *J. Am. Chem. Soc.* **2020**, *142*, 19001–19005; b) B. Han, Y. Guo, Y. Huang, W. Xi, J. Xu, J. Luo, H. Qi, Y. Ren, X. Liu, B. Qiao, T. Zhang, *Angew. Chem., Int. Ed. Engl.* **2020**, *59*, 11824-11829.

[5] H. Wei, X. Liu, A. Wang, L. Zhang, B. Qiao, X. Yang, Y. Huang, S. Miao, J. Liu, T. Zhang, *Nat. Communications* **2014**, *5*, 5634-5641.

[6] S. Li, Y. Xu, Y. Chen, W. Li, L. Lin, M. Li, Y. Deng, X. Wang, B. Ge, C. Yang, S. Yao, J. Xie, Y. Li, X. Liu, D. Ma, *Angew. Chem., Int. Ed. Engl.* **2017**, *56*, 10761-10765.

[7] N. C. Nelson, L. Chen, D. Meira, L. Kovarik, J. Szanyi, *Angew. Chem., Int. Ed. Engl.* **2020**, *59*, 17657-17663.

[8] N. Tang, Y. Cong, Q. Shang, C. Wu, G. Xu, X. Wang, *ACS Catal.* **2017**, *7*, 5987-5991.

[9] Z. Zhang, Y. Zhu, H. Asakura, B. Zhang, J. Zhang, M. Zhou, Y. Han, T. Tanaka, A. Wang, T. Zhang, N. Yan, *Nat. Communications* **2017**, *8*, 16100.

[10] C. K. Narula, L. F. Allard, G. M. Stocks, M. Moses-DeBusk, *Sci. Rep.* **2014**, *4*, 1-6.

[11] R. Lang, X. Du, Y. Huang, X. Jiang, Q. Zhang, Y. Guo, K. Liu, B. Qiao, A. Wang, T. Zhang, *Chem. Rev.* **2020**, *120*, 11986-12043.

[12] a) Z. Guo, S. H. Lim, W. Chu, Y. Liu, A. Borgna, *ACS Sustainable Chem. Eng.* **2020**, *8*, 10747-10755; b) W. Luo, M. Sankar, A. M. Beale, Q. He, C. J. Kiely, P. C. Bruijnincx, B. M. Weckhuysen, *Nat. Communications* **2015**, *6*, 1-10.

[13] a) R. T. Hannagan, G. Giannakakis, M. Flytzani-Stephanopoulos, E. C. H. Sykes, *Chem. Rev.* **2020**, *120*, 12044-12088; b) T. Zhang, A. G. Walsh, J. Yu, P. Zhang, *Chem. Soc. Rev.* **2021**, *50*, 569-588; c) J. Mao, J. Yin, J. Pei, D. Wang, Y. Li, *Nano Today* **2020**, *34*, 1-15.

[14] Y. Wang, H. Arandiyan, J. Scott, K.-F. Aguey-Zinsou, R. Amal, *ACS Appl. Energy Mater.* **2018**, *1*, 6781-6789.

[15] a) G. Liang, L. He, M. Arai, F. Zhao, *ChemSusChem* **2014**, *7*, 1415-1421; b) Z. Guo, D. Liu, S. H. Lim, Y. Liu, W. Chu, *Green Chem.* **2019**, *21*, 5999-6011; cH. Arandiyan, Y. Wang, J. Scott, S. Mesgari, H. Dai, R. Amal, *ACS Appl. Mater. Interfaces* **2018**, *10*, 16352-16357.

[16] J. Han, J. Lu, M. Wang, Y. Wang, F. Wang, *Chin. J. of Chem.* **2019**, *37*, 977-988.

[17] a) G. Meng, J. Sun, L. Tao, K. Ji, P. Wang, Y. Wang, X. Sun, T. Cui, S. Du, J. Chen, D. Wang, Y. Li, *ACS Catalysis* **2021**, *11*, 1886-1896; b) X. Zhang, G. Cui, H. Feng, L. Chen, H. Wang, B. Wang, X. Zhang, L. Zheng, S. Hong, M. Wei, *Nat. Communications* **2019**, *10*, 5812; c) K. Mori, T. Sano, H. Kobayashi, H. Yamashita, *J. Am. Chem. Soc.* **2018**, *140*, 8902-8909.

[18] C. Li, G. Xu, C. Wang, L. Ma, Y. Qiao, Y. Zhang, Y. Fu, *Green Chem.* **2019**, *21*, 2234-2239.

[19] Y. Ren, Y. Tang, L. Zhang, X. Liu, L. Li, S. Miao, D. Sheng Su, A. Wang, J. Li, T. Zhang, *Nat. Communications* **2019**, *10*.

[20] Y. Peng, Z. Geng, S. Zhao, L. Wang, H. Li, X. Wang, X. Zheng, J. Zhu, Z. Li, R. Si, J. Zeng, *Nano Lett.* **2018**, *18*, 3785-3791.

[21] Z. Xu, N. Wang, W. Chu, J. Deng, S. Luo, *Catal. Sci. Tech.* **2015**, *5*, 1588-1597.

[22] Z. Guo, J. E. Zheng, Y. Liu, W. Chu, *Appl. Catal., A* **2018**, *555*, 1-11.

[23] a) W. Wang, W. Chu, N. Wang, W. Yang, C. Jiang, *Int. J. Hydrogen Energy* **2016**, *41*, 967-975; b) J. Li, Y. Zhou, X. Xiao, W. Wang, N. Wang, W. Qian, W. Chu, *ACS Appl. Mater. Interfaces* **2018**, *10*, 41224-41236.

[24] X. Xiao, J. Wang, J. Li, H. Dai, F. Jing, Y. Liu, W. Chu, *Int. J. Hydrogen Energy* **2021**, 33107-33119.

[25] P. A. Lazaridis, S. A. Karakoulia, C. Teodorescu, N. Apostol, D. Macovei, A. Panteli, A. Delimitis, S. M. Coman, V. I. Parvulescu, K. S. Triantafyllidis, *Appl. Catal., B* **2017**, *214*, 1-14.

[26] a) B. Zhang, X. Li, Q. Wu, C. Zhang, Y. Yu, M. Lan, X. Wei, Z. Ying, T. Liu, G. Liang, F. Zhao, *Green Chem.* **2016**, *18*, 3315-3323; b) Y. Li, Y. Liao, X. Cao, T. Wang, L. Ma, J. Long, Q. Liu, Y. Xua, *Biomass Bioenergy* **2015**, *74*, 148-161; c) G. Liang, L. He, H. Cheng, W. Li, X. Li, C. Zhang, Y. Yu, F. Zhao, *J. Catal.* **2014**, *309*, 468-476.

[27] Y. Du, Y. Zhu, S. Xi, P. Yang, H. O. Moser, M. B. H. Breese, A. Borgna, *J. Syn. Rad*. **2015**, 22, 839-843.

[28] B. Ravel, M. Newville, *J. Syn. Rad*. **2005**, 12, 537-541.

Table of Content:

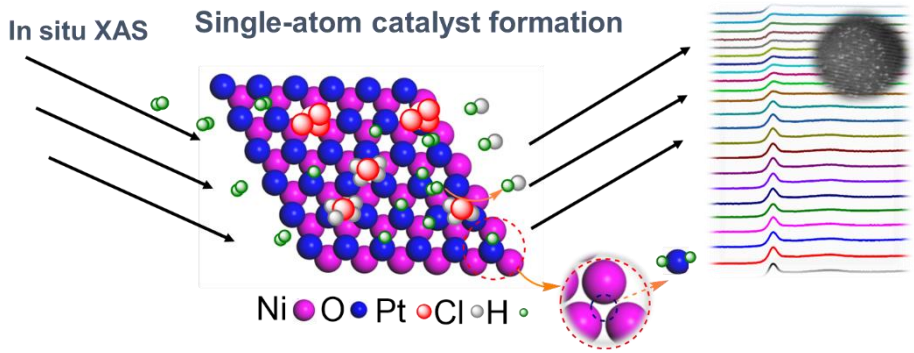

Reduction environment induced anti-Ostwald effect

The reduction environment induced anti-Ostwald effect was observed and identified to be the key for the formation of single atomic Pt on the confined nickel surface. *In situ* XAS experiments and DFT simulation revealed the general principle for a single-atom catalyst preparation over the confined metallic surface.